



## Research Paper

# Solid oxide fuel cells fed with dry ethanol: The effect of a perovskite protective anodic layer containing dispersed Ni-alloy @ FeOx core-shell nanoparticles



M. Lo Faro <sup>a,\*</sup>, R.M. Reis <sup>b</sup>, G.G.A. Saglietti <sup>c</sup>, V.L. Oliveira <sup>c</sup>, S.C. Zignani <sup>a</sup>, S. Trocino <sup>a</sup>, S. Maisano <sup>a</sup>, E.A. Ticianelli <sup>c</sup>, N. Hodnik <sup>d</sup>, F. Ruiz-Zepeda <sup>d</sup>, A.S. Aricò <sup>a</sup>

<sup>a</sup> Institute for Advanced Energy Technologies "Nicola Giordano" (ITAE) of the Italian National Research Council (CNR), Via Salita S. Lucia sopra Contesse 5, 98126 Messina, Italy

<sup>b</sup> Departamento de Engenharia Química - UTFPR, Avenida Monteiro Lobato, CEP 84016210, s/n, Km 04 - Ponta Grossa, Brazil

<sup>c</sup> Instituto de Química de São Carlos - USP, Av. Trab. São-carlense, 400, Brazil

<sup>d</sup> National Institute of Chemistry - Ljubljana, Slovenia

## ARTICLE INFO

## Article history:

Received 28 April 2017

Received in revised form 21 July 2017

Accepted 2 August 2017

Available online 8 August 2017

## Keywords:

Direct ethanol fuel cells

Solid oxide fuel cells

Ni-modified perovskite

Core-shell nanoparticles

Gadolinia-doped ceria

## ABSTRACT

Solid oxide fuel cells (SOFCs) based on conventional nickel-yttria stabilised zirconia (Ni-YSZ) anodes can not be fed directly with organic fuels because of the associated formation of carbon deposits. This work explores a simple approach to solve such relevant limiting factor that affects the direct utilization of conventional dry hydrocarbons in SOFCs. The approach consists in depositing a composite multifunctional electrocatalyst layer on the SOFC anode to work as an internal integrated fuel processor. This study investigates the direct oxidation of dry ethanol in the modified SOFC and provides an evaluation of cell performance. A protective layer based on a composite made of Ni-modified perovskite and gadolinia-doped ceria is coated on a conventional SOFC anode based on Ni-YSZ. Besides the oxygen storage properties of ceria, the composite electrocatalyst is characterized by the presence of dispersed Ni-alloy @ FeOx core-shell nanoparticles in the outer layers and surface basicity properties. Efficient dehydrogenation of ethanol, carbon deposition-free cracking reactions and internal reforming assisted by a H<sub>2</sub>/H<sub>2</sub>O "shuttle mechanism" appear as the key steps involved in the direct oxidation of the organic fuel at the modified SOFC anode. The best performance achieved for the dry ethanol-fed SOFC is about 0.65 W cm<sup>-2</sup> at 0.6 V and 800 °C. No carbon deposition is observed both on the Ni-YSZ supporting layer and protective Ni-doped perovskite layer after a durability test of more than 100 h.

© 2017 Elsevier B.V. All rights reserved.

## 1. Introduction

The market penetration of advanced technologies for distributed energy generation can be significantly enhanced by the development of highly efficient and reliable conversion devices such as fuel cells mainly fed with bio-alcohols [1,2]. Although Solid Oxide Fuel Cells (SOFCs) have the potentialities to be part of this new market, the present systems still suffer from relevant issues [3].

SOFCs are currently based on anode-supported planar cells made of Ni-YSZ supporting cermets [4]. This cell structure offers good robustness and reliability for operation with syngas and

methane internal reforming [5]. External fuel processing to syngas is instead required for larger molecular weight hydrocarbons, and an upstream desulphurisation process is needed for natural gas and other fuels of practical interest. However, this configuration is affected by several constraints [6]. In particular, i) a poor redox stability with an associated risk of electrode delamination from the electrolyte layer due to the dimensional mismatch between metallic nickel and Ni-oxide during the Ni<sup>0</sup>/NiO redox cycle, ii) a very poor flexibility for the direct utilization of dry hydrocarbons which is replaced by fuel processing through external reforming/partial oxidation, iii) internal reforming is only possible in the case of pure methane and not for natural gas, iv) limited tolerance to sulphur contaminants (few ppm); this requires the use of a large desulphurizer. Although several new materials have been demonstrated to be appropriate for application in SOFCs [5,7,8], in the short-period, the replacement of the Ni-YSZ based anode appears not feasible

\* Corresponding author.

E-mail address: [lofaro@itaecnr.it](mailto:lofaro@itaecnr.it) (M. Lo Faro).

due to the high industrial risk associated with a new production chain for novel materials-based cells which have not yet shown proper mechanical robustness. A possible strategy to overcome the limitations of commercial cells is regarding the anode coating with a protective layer, which is active towards catalytic conversion of the organic fuel and more tolerant to sulphur contaminants while avoiding to introduce relevant ohmic drop. Previous studies carried out in our laboratory on bimetallic cermets, used as a protective layer, have already shown a significant influence on improving the stability of the SOFC cells towards the direct utilization of ethanol [9]. However, still some formation of carbon nanofibers on bimetallic alloys, during prolonged operation with dry hydrocarbons, can compromise the long-term stability of these devices. Whereas, oxide-layers containing encapsulated Ni particles on the surface are in principle less affected by carbon deposition [8,10]. In this work, the utilization of a low Ni content modified perovskite in combination with gadolinia doped ceria (CGO) is investigated as a protective layer for the anode of a commercial-type cell fed with ethanol.

The use of perovskite anodes in SOFCs has been the focus of several studies [11–15]. Different approaches have been proposed including i) perovskite formulations that are chemically stable under reducing conditions [16], but require high operating temperatures ( $>800^{\circ}\text{C}$ ) or ii) perovskites characterized by high electronic or ionic conduction allowing to work at intermediate temperatures ( $650^{\circ}\text{C}$ – $800^{\circ}\text{C}$ ) but requiring modification or stabilization treatments [17]. Moreover, redox stable perovskites containing exsolved metal particles on the surface from B-site doping have recently attracted relevant interest as anode materials [18–25].

The investigated approach in this study differs from the above mentioned configurations since the perovskite structure, based on a strontium doped lanthanum ferrite-cobaltite, is decorated on the surface with Ni nanoparticles and successively stabilised by specific thermal treatments corresponding to the pre-conditioning treatments of a SOFC operating at  $800^{\circ}\text{C}$  (i.e. static air up to  $800^{\circ}\text{C}$  and then diluted  $\text{H}_2$  at the same temperature). In particular, a ceramic composite made of Ni-modified perovskite and CGO is coated on the supporting anode of a conventional cell. Therefore, the composite of Ni-modified perovskite and CGO is used as catalytic layer in order to convert the alcohol in syngas or other reaction intermediates to minimize the risk of carbon formation. We show that such simple modification of the SOFC cell can provide significantly enhanced activity towards the direct utilization of dry ethanol without the relevant occurrence of carbon deposits.

## 2. Experimental

Low Ni content modified perovskite mixed to CGO has been prepared by an incipient wetness method at  $50^{\circ}\text{C}$  using  $\text{La}_{0.6}\text{Sr}_{0.4}\text{Fe}_{0.8}\text{Co}_{0.2}\text{O}_3$  PRAXAIR raw powders ( $11.19\text{ m}^2\text{ gr}^{-1}$ ) and 10 wt.% of Ni as Ni-nitrate (Aldrich) solution (0.5 M) in water. The wet raw powders were dried at  $110^{\circ}\text{C}$  for 2 h and then calcined in air at  $500^{\circ}\text{C}$  for 5 h. The resulting raw powders were grinded for 20 h with  $\text{Gd}_{0.1}\text{Ce}_{0.9}\text{O}_{2-\delta}$  (CGO, Praxair,  $38.92\text{ m}^2\text{ gr}^{-1}$ ) with a weight ratio of 70:30 in the presence of ethanol. This composite material was spray-coated onto a Ni-YSZ anode surface of a conventional SOFC cell. This was thermally treated at  $800^{\circ}\text{C}$  in air and thereafter in hydrogen during cell conditioning. Hereafter this composite layer (Ni-modified perovskite and  $\text{Gd}_{0.1}\text{Ce}_{0.9}\text{O}_{2-\delta}$ ) will be referred as “protective layer” or “pre-layer”. Ni-modified perovskite powders, treated under conditions similar to the protective layer that is applied on the anode, were characterized by X-ray diffraction (XRD – PANalytical X'Pert), Electron Transmission Microscopy (TEM – FEI) equipped with Energy dispersive X-ray analyser (EDX), and X-ray photoelectron spectroscopy (XPS – PHI 5800-1).

The composition of the nanostructure was investigated by scanning transmission electron microscopy (STEM) carried out in a Cs corrected microscope CF-ARM Jeol operated at 200 kV, equipped with a SSD Jeol EDX spectrometer.

The electrochemical behaviour of a commercial SOFC coated with the protective layer and fed directly with absolute ethanol ( $\geq 99.5\text{ vol.}\%$ ) was investigated. Electrochemical experiments were carried out in a set-up including a furnace for high temperature tests, syringe pump for liquid ethanol and mass flow controller for the gases (hydrogen and inert gas) used during the cell pre-conditioning and as carrier during the operation with liquid ethanol. The cell used for the electrochemical experiment consisted of button cell ( $2\text{ cm}^2$ ) laser-cut from a large area anode-supported cell ( $100\text{ cm}^2$ ) and with the architecture and composition referred to Ni-YSZ/YDC/YSZ/LSFC; YDC refers to Yttria doped Ceria and the other components were defined above. Gold wires were attached to the anode by using a gold paste and thermally treated at  $450^{\circ}\text{C}$  for curing and subsequent annealing the electrical contacts. The anode was spray coated with the protective layer powders to obtain a deposit of approximately  $4\text{ }\mu\text{m}$  thick. Then, the cell was sealed onto an alumina tube with the anode exposed to the inner part of tube and the cathode exposed to the external static air. Gold wires were thus attached to the cathode side and thermally treated as above described for the anode. The sealing was assured by a ceramic paste (AREMCO 516) that was annealed with a specific thermal treatment procedure suggested by the manufacturer in the presence of inert gas fed into the anode. The cell temperature was measured by a thermocouple in contact with the cathode. After reaching the operating temperature ( $800^{\circ}\text{C}$ ) in the presence of air, the cell was initially fed at the anode with  $\text{N}_2$  and then with an  $\text{N}_2/\text{H}_2$  mixture with a gradual transition to pure  $\text{H}_2$ . This procedure allowed to reduce both the Ni nanoparticles decorated on the perovskite surface and the  $\text{NiO}$  of the supporting SOFC anode. The electrochemical experiments were carried out by feeding a constant flow of ethanol. This was set at  $4.5\text{ cc min}^{-1}$  or at  $6.4\text{ cc min}^{-1}$  ethanol vapour, that was in excess to the amount required by the faradaic reaction. The sealing properties were checked by a thermocamera [26]. An AUTOLAB PGSTAT30 Metrohm potentiostat equipped with a 20 A booster and a frequency-response analyser module for impedance spectroscopy was used for the electrochemical investigation. The polarization curves were carried out from OCV to 0.5 V. EIS spectra were obtained at 0.7 V in the frequency range from  $10\text{ mHz}$  to  $1\text{ MHz}$  with an applied AC-voltage amplitude of  $10\text{ mV rms}$ . The outlet stream was collected in a cold ice trap and then analysed by GC-MS spectrometry (AGILENT 7890A+5975C) equipped with a column DB-WAXETR (Agilent). The gas stream after the condenser was also analysed by using micro-GC (Varian – CP4900) and Mass spectroscopy (Pfeiffer – ThermoStar GSD 320T). The morphology of the cell was then studied by scanning electron microscopy (LEO 440 SEM-EDX system (Leica-Zeiss, Cambridge, England)).

## 3. Results

### 3.1. Ex-situ physico-chemical analysis of the protective layer electrocatalyst

**Fig. 1** shows a comparison between the X-ray diffraction of the LSFCO precursor and the Ni-modified perovskite after specific thermal treatments (calcination at  $500^{\circ}\text{C}$  and subsequent reduction at  $800^{\circ}\text{C}$ ). Two new phases ascribed to a Co- and Fe-partially depleted perovskite based on a  $\text{SrFeLaO}_4$ -type structure showing a Ruddlesden-Popper phase (i.e.  $\text{K}_2\text{NiF}_4$ -type oxides [27,28]) and to an  $\alpha\text{-Fe}_{100-y-z}\text{Co}_y\text{Ni}_z\text{O}_x$  oxide compound containing an excess of Fe [29–31], were formed as consequence of the thermal treatments. These caused quite significant exsolution of Co and partial exsolu-

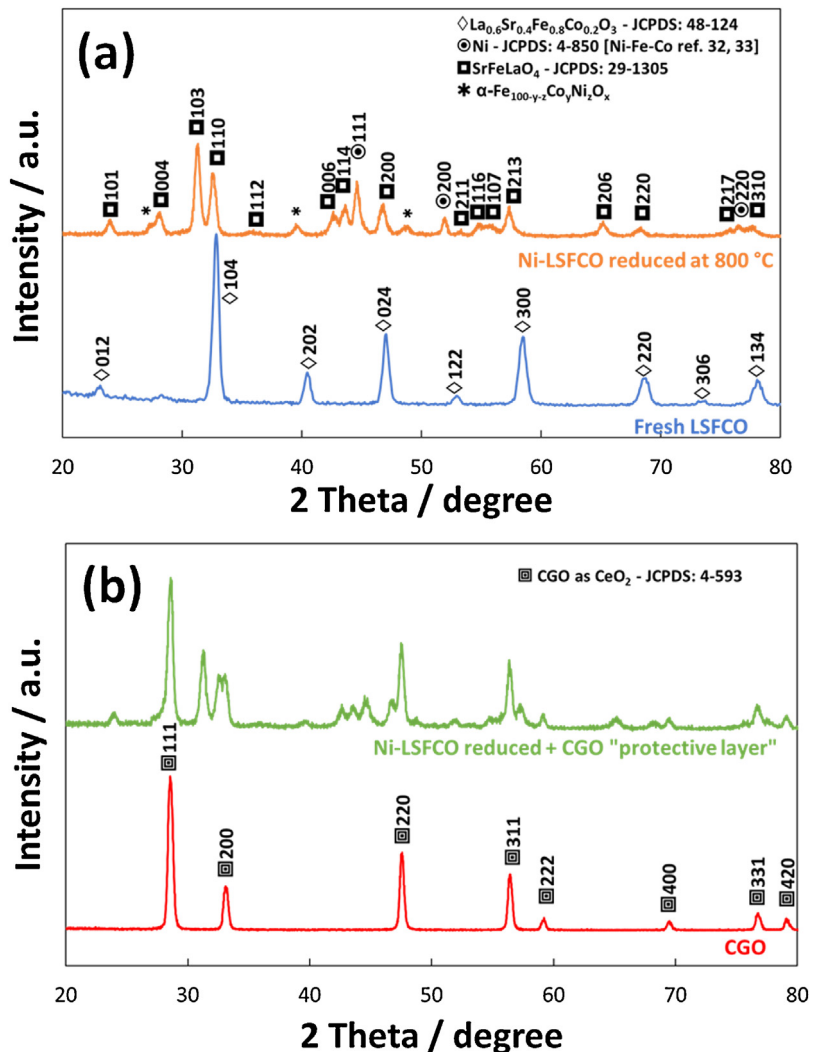


**Fig. 1.** a) X-ray diffraction of commercial fresh LSFCO and Ni-modified perovskite after the thermal treatment consisting in calcination at 500 °C and subsequent reduction at 800 °C. b) composite pre-layer compared to raw CGO powders.

tion of Fe from the perovskite. The Co- and Fe-depleted structure of the perovskite did not show any further reaction. A metallic Ni alloy (NiFeCo) with face centered cubic structure likely occurs according to a slight shift towards low Bragg angles was observed [32,33]. As a reference, the XRD patterns of the LSFCO perovskite structure, which was not doped with Ni subjected to the same thermal treatments as for the Ni-modified perovskite, is shown in the supplementary information (Fig. S1). A modification of the LSFCO after the high-temperature reduction into a SrFeLaO<sub>4</sub> with Ruddlesden-Popper structure together with an exsolved FeCo alloy is observed.

Bright field TEM images provide information on the morphology of the Ni-modified perovskite used for the pre-layer. Fig. 2a–c shows aggregates of large perovskite particles supporting fine Ni-Fe-Co-based particles (see below) of about 20 nm originated from the thermal reduction treatment of the perovskite decorated with Ni-nitrate. Fig. 2d shows a dark field micrograph of a typical nanosized particle on the surface where EDX line scanning (Fig. 2e) of the chemical elements was carried out. Fig. 2f shows another nanosized particle and a suitable portion of the support where EDX mapping was made. These nanosized particles dispersed on the surface are slightly more oxidized on the surface. The EDX line scan (Fig. 2d, e) and the mapping of the nanoparticles (Fig. 2f) show an increase of the oxygen content in the outermost layers (shell) whereas oxygen appears less evident in the core. Ni appears less

present in the outermost layers but highly concentrated in the core of the nanosized particles. Thus, the nanoparticles appear slightly enriched of Fe beside oxygen on the surface (Fig. 2e, f). This appears as a unique core-shell structure different from after exsolved perovskite electrocatalysts which have also been identified as suitable oxidation promoters in SOFCs [18]. Moreover, these evidence indicate a promoting role of Ni in favouring the partial exsolution of Fe and Co from the perovskite and their reprecipitation and segregation around the nanosized Ni particles on the surface forming a core-shell structure. This evidence is also in line with XRD analysis indicating metallic Ni-Co-Fe ternary alloy (observed essentially in the core of the nanosized particles from HR-TEM) and a less crystallised  $\alpha$ -Fe<sub>100-y-z</sub>Co<sub>y</sub>Ni<sub>z</sub>O<sub>x</sub> phase with minimal Ni content observed on the surface of the nanosized particles together with the Co-Fe depleted perovskite support. Therefore, the absence of metallic Ni in the shell of these dispersed particles corroborates the absence of carbon formation in the cell after prolonged operation with dry ethanol (see below). The EDX mapping of catalyst carried out on the support showed a clear depletion of Co and essentially no Ni embedded in the support (Fig. 2f).

High resolution transmission electron microscopy analysis of the Ni-modified perovskite and CGO composite (Fig. S2) shows an appropriate mixing on a nanoscale as also confirmed by the EDX mapping (Fig. S3).

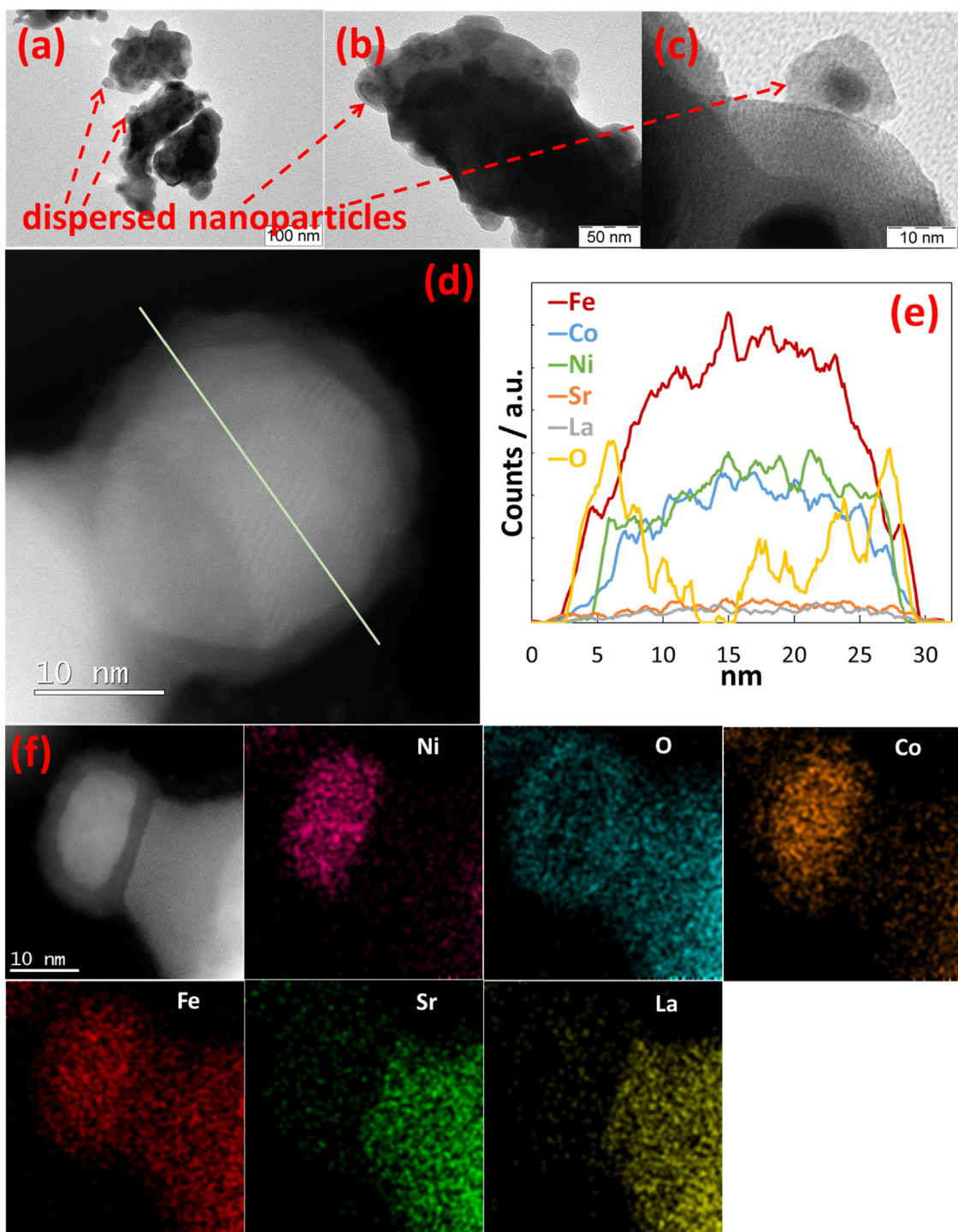


**Fig. 2.** Bright field TEM images of Ni-modified LSFCo after thermal treatments (calcination at 500 °C and reduction at 800 °C) obtained at different magnifications (a–c). High magnification high angle annular dark field image of a dispersed nanosized core-shell particle (d) and EDX line scan (e). EDX mapping of a portion of catalyst including a nanosized particle and support (f).

The mechanism of formation of the core-shell nanostructures on the perovskite surface is discussed below. During the thermal treatment, the Ni clusters react with the perovskite substrate; in parallel, exsolution of Fe and Co atoms from the B-site of the  $\text{ABO}_3$  perovskite structure occurs to form nanoparticles of Ni-Fe-Co alloy upon reduction with segregation of an oxide phase i.e.  $\alpha\text{-Fe}_{100-y-z}\text{Co}_y\text{Ni}_z\text{O}_x$  in the outermost layers of the nanoparticle. The perovskite support remains depleted of Co and partially depleted in Fe. Such particular nanostructure is characterized by

good electronic percolation through the Ruddlesden-Popper phase (i.e.  $\text{SrFeLaO}_4$ ) support whereas the absence of metallic Ni in the outermost layers of the nanoparticle avoids the cracking of organic fuels. It is anticipated that no significant increase of ohmic resistance with respect to a conventional cell was observed being conductivity mainly assured by the MIEC (i.e. mixed ionic and electronic conductivity) properties of  $\text{SrFeLaO}_4$  phase. Whereas, the dispersed nanoparticles are expected to have proper conduction according to the metal core as evidenced from XRD.

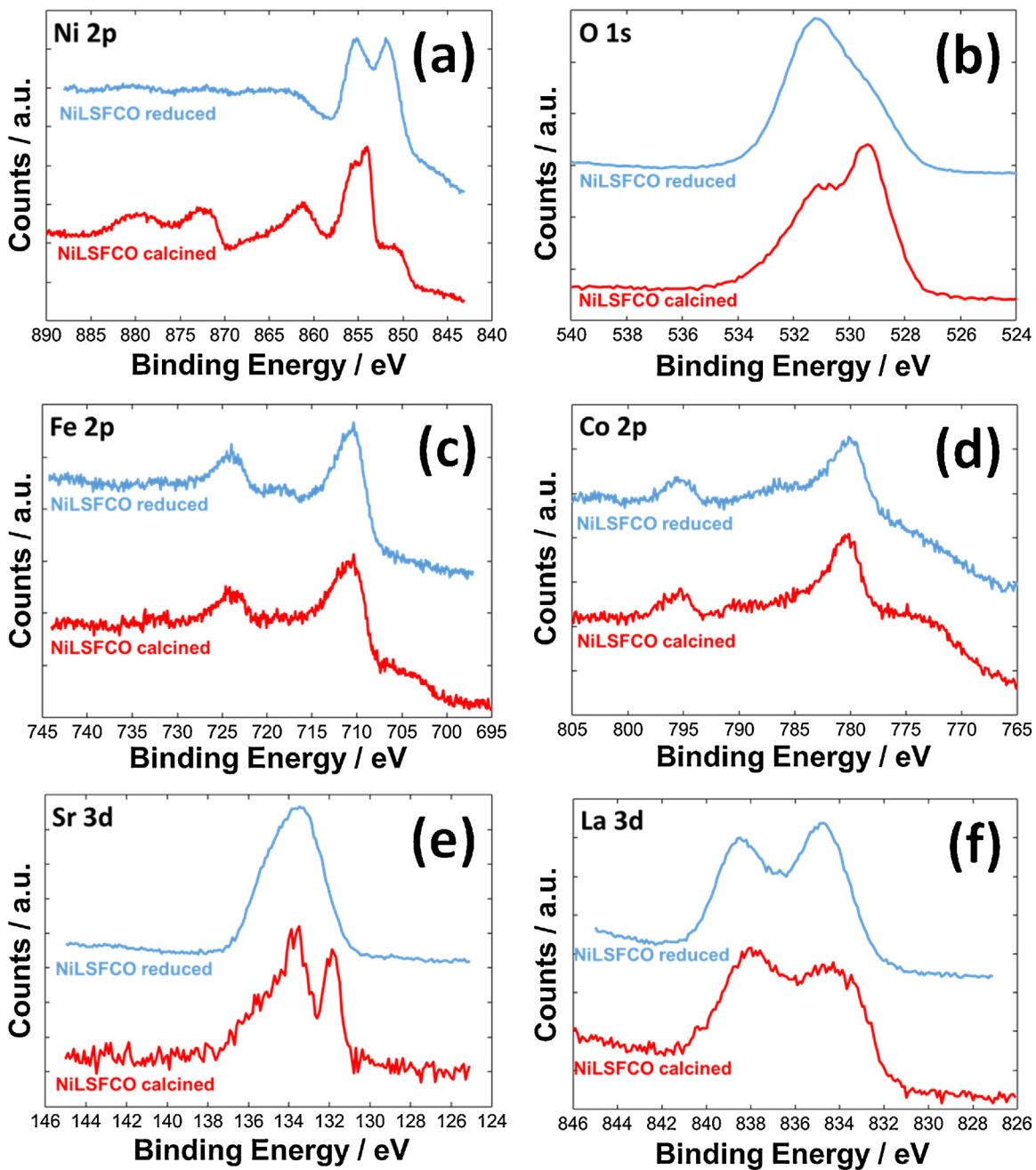
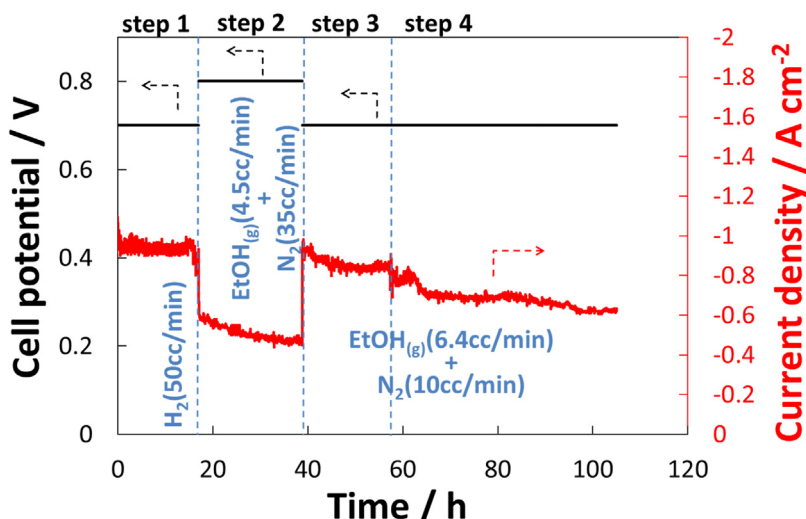


Fig. 3. Comparison of XPS multiplex spectra of element included in the Ni-modified LSFCO after thermal treatments.

XPS survey spectra of the modified perovskite and high resolution spectra of the C 1s region are shown in Fig. S4a, b (Supporting information). The Ce 3d spectra of calcined and reduced CGO are shown in Fig. S4c. Ce<sup>3+</sup> species are clearly observed in the reduced sample whereas Ce<sup>4+</sup> is present in the calcined catalyst. High resolution XPS analysis of the elements occurring on the modified perovskite is shown in Fig. 3a–f. The analysis of the Ni 2p region is made difficult by the overlapping with the La 3d<sub>3/2</sub> signal occurring at the 851.5 eV for La-oxide materials [34]. However, comparison of calcined and reduced (final) samples allows getting insights into the electronic structure of this material. The Ni 2p spectrum (Fig. 3a) of the calcined sample shows the occurrence of the typical profile of paramagnetic NiO with the main Ni 2p<sub>3/2</sub> line occurring at 854.5 eV [34]. The shoulder at 851 eV is associated to La 3d<sub>3/2</sub> of the perovskite (Fig. 3a). Whereas the reduced sample shows a shift to lower binding energy (B.E.) with the occurrence of the Ni

2p<sub>3/2</sub> at about 852 eV clearly indicating the formation of metallic Ni (Fig. 3a). Moreover, the presence of a Ni 2p<sub>3/2</sub> peak at 855.5 eV would indicate the presence of Ni-hydroxide species with electronic characteristics similar to the Ni in  $\alpha$ -Fe<sub>100-y-z</sub>Co<sub>y</sub>Ni<sub>z</sub>O<sub>x</sub> often referred as tertiary oxyhydroxydes [31,34]. Deconvolution of the Ni2p spectra (Fig. S5) confirms essentially such evidence. The typical Ni2p profile of paramagnetic NiO is observed in the calcined sample. The shoulder at 851.5 eV of La 3d<sub>3/2</sub> is partially masked in the case of metallic Ni formation. The relative intensities of the Ni 2p<sub>3/2</sub> peaks in the reduced sample after deconvolution shows a slight prevalence of the oxidized Ni peak at higher binding energy (Ni(OH)<sub>2</sub>). These results are in agreement with the fact that metallic Ni is mainly in the core of the nanoparticles being the analysis depth of XPS about 5 nm.

The decrease of the O 1s signal at 529 eV in the reduced sample (Fig. 3b) associated to the transition metal oxides compared



**Fig. 4.** Endurance test carried out on a SOFC coated with a Ni-perovskite protective layer operating in H<sub>2</sub> and dry ethanol. Red line is referred to the current density whereas black line is related to the cell potential. (For interpretation of the references to colour in this figure legend, the reader is referred to the web version of this article.)

**Table 1**

Quantitative distribution of the different elements on the surface of the Ni-LSFCO catalyst after specific thermal treatments.

	Ni 2p at.%	La 3d at.%	Sr 3d at.%	Fe 2p at.%	Co 2p at.%
NiLSFCO calcined	51.1	3.2	3.9	28.2	13.6
NiLSFCO reduced	46.8	5.9	18.2	20.7	8.4

to the peak at 531 eV, mainly related to the adventitious oxygen (Fig. S5), confirms the presence of partially reduced metals and the increased capability of the reduced sample to interact with organic oxygenated species (see increase of C1s peak at 289.5 eV, Fig. S4b Supplementary information).

Fe 2p and Co2p (Fig. 3c, d) are still mainly in an oxidation state in the outermost layer after the hydrogen reduction indicating their prevailing content in the  $\alpha$ -Fe<sub>100-y-z</sub>Co<sub>y</sub>Ni<sub>z</sub>O<sub>x</sub> shell. The electronic properties of the main structure of the perovskite do not appear significantly modified. Some interconversion between two redox states for the La in the conventional perovskite structure causes the occurrence of a larger intensity for the peak at 838 eV in the calcined perovskite. This may result from the partial overlapping of La 3d<sub>3/2</sub>/La 3d<sub>5/2</sub> of higher La oxidation states and lower valence state of lanthanum species. The occurrence of the expected ratio from the spin-orbit coupling (3/2) between La 3d<sub>5/2</sub> and La 3d<sub>3/2</sub> in the reduced sample indicates lower interconversion of redox states as expected for La in SrFeLaO<sub>4</sub>. The increase of Sr occurrence on the surface is indicative of an increased basicity for the support as confirmed by the data reported in Table 1.

Quantitative XPS data show essentially a strong increase of the Sr content in the reduced sample producing an increase of surface basicity. It was observed in a previous work that the surface basicity of the anode surface can play a paramount role in mitigating the formation of carbon deposits [35]. This variation is due to the formation of a new phase associated to SrFeLaO<sub>4</sub> with redistribution of the perovskite elements on the surface. The prevailing concentration of Ni on the surface confirms the homogeneous distribution of the nanosized Ni-based particles on the support according to the EDX and TEM analysis. Interestingly, the overall content of Fe and Co elements on the perovskite surface decreases upon reduction. As discussed above, most of the exsolved Fe and Co atoms contribute to form the Ni-Fe-Co alloy core of the nanoparticles which is in part shielded by oxygen atoms in the outermost layers (Fig. 3e).

### 3.2. Electrochemical studies

To determine the stability of the Ni-modified perovskite-based cell under dry ethanol feed, a durability test of 100 h (Fig. 4) was carried out after the conditioning procedure. The first step regarded an operation of the cell in H<sub>2</sub> (50 cc min<sup>-1</sup>) at 0.7 V. The cell showed a large initial spike of current for a short period after that the SOFC device achieved a steady state condition at an average current density of about 0.95 A cm<sup>-2</sup> (step 1).

Subsequently, dry ethanol was fed to the cell with a low flow rate (4.5 cc min<sup>-1</sup>) together with inert gas (N<sub>2</sub>, 35 cc min<sup>-1</sup>); nitrogen was used as a carrier. Under this condition, the cell was initially operated at 0.8 V (step 2). The current density decreased slightly to reach an average value of about 0.45 A cm<sup>-2</sup>. The observed current density oscillations could be in part related to the fluctuation of the ethanol flow caused by the syringe pump.

Afterward, the durability test was continued at 0.7 V and the ethanol feed was increased (6.4 cc min<sup>-1</sup>) using a lower flow rate of N<sub>2</sub> in step 3 (10 cc min<sup>-1</sup>). This was the minimum flow rate that could be precisely set with the used mass flow controller. An increase of performance compared to step 2 was observed during the first 20 h (step 3). A slow relaxation of the current density towards a steady-state value of 0.9 A cm<sup>-2</sup> almost comparable to the steady-state current density in H<sub>2</sub> was observed (step 3).

At the end of steps 1, 2 and 3, electrochemical diagnostics consisting in polarization curves and ac-impedance analyses were carried out. After the electrochemical diagnostics were conducted at the end of step 3, the cell showed a steep decrease of current density to 0.7 A cm<sup>-2</sup> during operation at 0.7 V (step 4). Such a rapid change should not be associated with a progressive degradation of the anode but probably to the occurrence of some diffusion constraints during previous cell polarization experiments (see below in step 2) [36].

The conversion of ethanol ranged between 26% at 0.8 V (in step 2) and 30% at 0.7 V (in step 3). The low fuel utilization is essentially related to the button cell configuration and the minimum ethanol feed rate of the liquid pump. Whereas the nitrogen carrier flow was optimised to avoid excessive dilution of ethanol with consequent decrease of partial pressure. However, the fuel utilization conditions used here are not much lower than those of a practical SOFC stack. Thus, the results observed for the present button cell are certainly of practical interest.

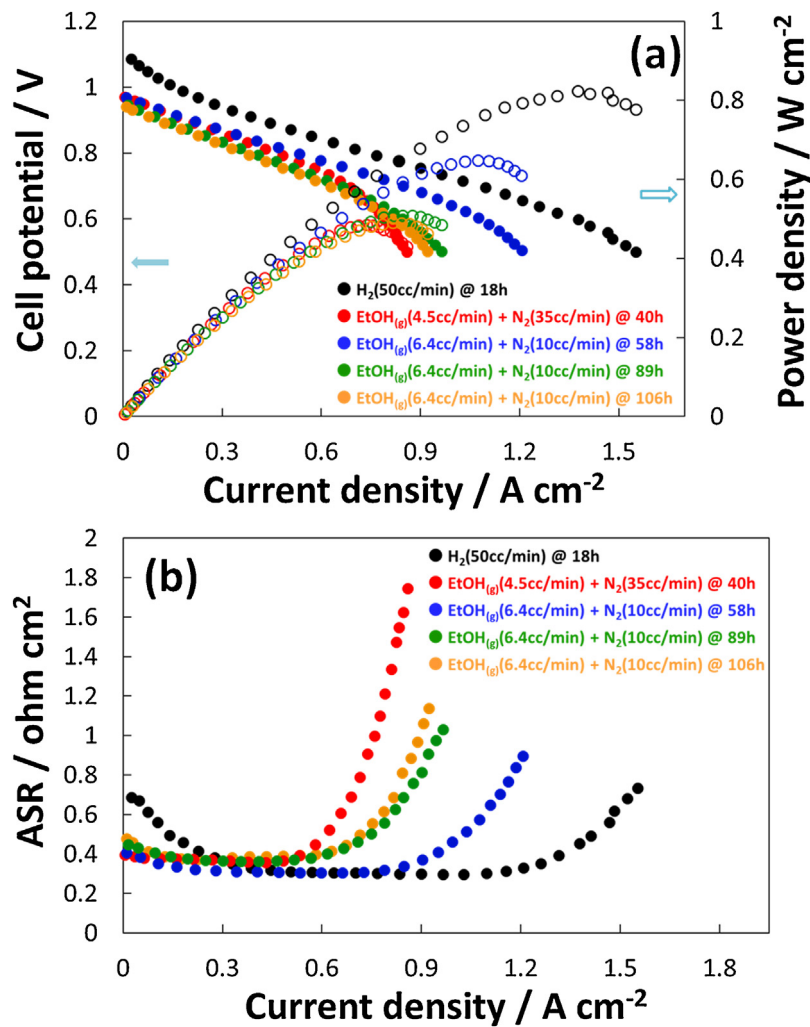


**Fig. 5.** a) Polarization and power density curves carried out during the endurance test. b) Area specific resistance determined from the slope of voltage vs. current density.

The same experiment was carried out with an uncoated cell, i.e. the same cell without any protective layer. A rapid deactivation and the occurrence of carbon deposits were observed (Figs. S6 and S7 of Supplementary information).

As above discussed, during the endurance test reported in Fig. 4, between different steps or at some time intervals, electrochemical diagnostics, consisting of I-V polarization curves and electrochemical impedance spectroscopy (EIS) studies at the specific potentials of 0.8 V and 0.7 V, were carried out. Such electrochemical analysis was useful to investigate the mechanism of the reactions occurring at the anode during the electrochemical operation and the effect of partial pressure for the ethanol stream.

Fig. 5a shows a comparison of the various polarization curves recorded during the endurance test. The I-V curve obtained in the presence of H<sub>2</sub> showed an OCV comparable to that observed for the uncoated cell (1.08 V) [37]. The curve was slightly affected by activation losses at low current densities. A wide ohmic region with a linear variation of potential vs. current was observed for the I-V curve in H<sub>2</sub> (Fig. 5a). The ohmic resistance remained substantially constant. A maximum power density of 0.82 W cm<sup>-2</sup> @ 0.56 V was achieved in hydrogen. When dry ethanol was fed to the cell, and the I-V curve was collected at 40 h (end of step 2 in Fig. 4), the open circuit voltage decreased by more than 100 mV (Fig. 5a). However, no relevant activation losses are displayed by the I-V curves excluding the decrease of OCV. The similar slope in the linear region of the polarization curves (Fig. 5) in H<sub>2</sub> and

ethanol indicates that the ohmic resistance is almost the same for these operating conditions. Increased mass transport constraints in the presence of ethanol feed at high current densities may be associated with the diffusion limitations for the large organic molecule, compared to H<sub>2</sub>, to reach specific catalytic sites and for the reaction products to evolve from the electrode layer. These diffusion limitations were recorded already at 600–700 mA cm<sup>-2</sup> as observed by a rapid increase of polarization resistance (Fig. 5b). Excluding the low OCV, the absence of relevant activation losses is an indication that the electrocatalyst used as protective layer is active towards the oxidation of dry ethanol. However, polarization curves can not provide indication if the oxidation reaction at the pre-layer proceeds up to the formation of the final products (i.e. H<sub>2</sub>O and CO<sub>2</sub>) rather than to syngas (i.e. H<sub>2</sub> and CO) or secondary products (e.g. methane, ethylene, acids or aldehydes). In principle, syngas can be more easily transported than large organic molecules through the pre-layer and oxidized electrochemically at the Ni-YSZ interface. In any case, according to the results obtained for the uncoated cell, the pre-layer seems to play a paramount role and the first reaction step should occur at this level.

When the ethanol partial pressure in the fuel stream fed to the anode was increased (step 3 in Fig. 4), the cell showed a significant increase in performance compared to the previous ethanol feed condition as recorded in the polarization curve at 58 h. Whereas, the OCV was essentially unchanged. This was the result of lower mass transport constraints in the presence of an increased ethanol

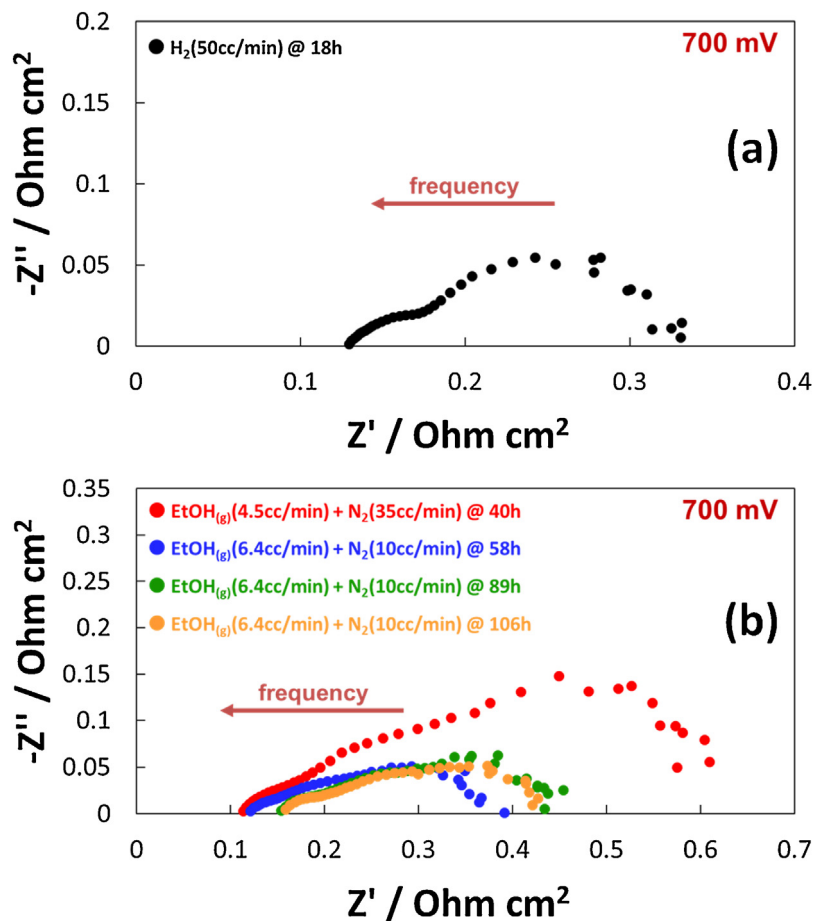


**Fig. 6.** Electrochemical Impedance Spectra (EIS) carried out during the endurance test: a) in  $\text{H}_2$  and b) under ethanol feed.

flow rate and partial pressure. A maximum power density of about  $650 \text{ mW cm}^{-2}$  @  $0.6 \text{ V}$  in a region mainly controlled by diffusion limitations was observed for the direct utilization of dry ethanol. Further I-V curves were carried out at increased times of operation (i.e. 89 h and 106 h) corresponding to step 4. The OCV slightly decreased during the endurance test (Fig. 4a) whereas the slope in the linear region did not vary significantly (Fig. 5a, b). The most significant performance loss was mainly due to the increase of diffusion constraints. Diffusion limitations appeared to occur at relatively high voltages (i.e. higher than  $0.7 \text{ V}$  and at relatively low currents, Fig. 5a, b). Possibly, this was one of the main effects causing the decay of current density observed in the endurance test (Fig. 4). Such issue could be associated with a loss of porosity with time or some occlusion effect produced by large organic molecules, which could explain the steep change in current density during operation with ethanol flow at around 60 h in Fig. 4 after the polarization experiments. The possibility that occlusion is caused by carbon deposition is disregarded here because of the absence of carbon formation (see below).

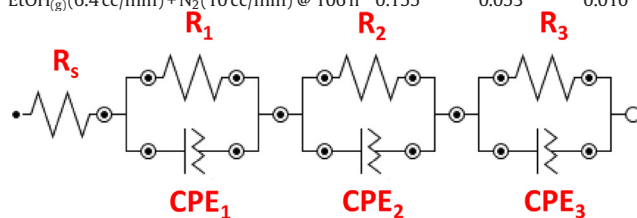
The EIS spectra, collected at  $700 \text{ mV}$ , are reported in Fig. 6a and b whereas the results of the data fitting for the spectra are summarized in Table 2. The high frequency intercept on the real axis provides the value of the series resistance ( $R_s$ ) which is associated with the ohmic characteristics of the cell. As seen in Table 2,  $R_s$  is relatively low in all cases ( $0.11\text{--}0.15 \Omega \text{ cm}^2$ ) and not significantly different from the uncoated cell [37]. It is derived that the interaction between the protective layer (i.e. Ni-modified perovskite) and the anodic support of cell (i.e. Ni-YSZ) has not caused any relevant increase of ohmic resistance across their interface. In the presence of  $\text{H}_2$  feed, the ac-impedance spectrum can be modelled by two

overlapping semicircles, which are well distinguished. The small semicircle at high frequency in Fig. 6a is mainly ascribed to the cathodic reaction characterized by a higher relaxation frequency than  $\text{H}_2$  oxidation for this type of SOFCs operating at  $800^\circ\text{C}$  [38]. The high frequency semicircle remains small also when ethanol is fed to the anode (Fig. 6b). This confirms that the semicircle is mainly related to the oxygen reduction. The large semicircle at low frequencies is instead attributed to the anodic process. Possibly, the presence of the pre-layer may have caused a slight increase of the polarization resistance for the hydrogen reaction. The EIS spectra of the SOFC fed with ethanol (Fig. 6b) showed a further semicircle at very low frequencies. According to the behaviour observed in the polarization curves, this may be assigned to the diffusion constraints related to the oxidation of ethanol. The size of the semicircle occurring at very low frequencies in Fig. 6b becomes significantly large when the ethanol partial pressure in the fuel stream is reduced and mass transport limitations are particularly relevant in the polarization curves in Fig. 5a. By increasing ethanol concentration, as for the spectrum at 58 h, both the second and third semicircles associated to the ethanol reaction decrease in size (enhanced reaction rate). However, after prolonged operation (89 h and 106 h), an increase of both series resistance and size of the semicircle related to mass-transport is observed. This is in accordance with the behaviour observed in the polarization curves. The corresponding equivalent circuit (inset of Table 2) is made by a resistance in series with two or three RQ components, where Q is a constant phase element (CPE) replacing the typical parallel capacitance associated with the interface. An additional consideration is that the constant phase elements (CPE) were used in the fitting pro-

**Table 2**

Data fitting for the EIS spectra collected during the endurance test.

	CPE <sub>1</sub>			CPE <sub>2</sub>			CPE <sub>3</sub>			
	R <sub>s</sub> ( $\Omega \text{ cm}^2$ )	R <sub>1</sub> ( $\Omega \text{ cm}^2$ )	Y <sub>1</sub> (mho $\text{cm}^{-2}$ )	n <sub>1</sub>	R <sub>2</sub> ( $\Omega \text{ cm}^2$ )	Y <sub>2</sub> (mho $\text{cm}^{-2}$ )	n <sub>2</sub>	R <sub>3</sub> ( $\Omega \text{ cm}^2$ )	Y <sub>3</sub> (mho $\text{cm}^{-2}$ )	n <sub>3</sub>
H <sub>2</sub> (50 cc/min) @ 18 h	0.129	0.048	0.301	0.640	0.153	0.324	0.779			
EtOH <sub>(g)</sub> (4.5 cc/min) + N <sub>2</sub> (35 cc/min) @ 40 h	0.113	0.056	0.020	0.769	0.197	0.216	0.782	0.236	1.70	0.987
EtOH <sub>(g)</sub> (6.4 cc/min) + N <sub>2</sub> (10 cc/min) @ 58 h	0.121	0.034	0.020	0.717	0.087	0.216	0.714	0.112	2.50	0.830
EtOH <sub>(g)</sub> (6.4 cc/min) + N <sub>2</sub> (10 cc/min) @ 89 h	0.153	0.053	0.010	0.687	0.110	0.217	0.705	0.113	2.70	0.810
EtOH <sub>(g)</sub> (6.4 cc/min) + N <sub>2</sub> (10 cc/min) @ 106 h	0.155	0.053	0.010	0.687	0.110	0.218	0.697	0.113	3.20	0.792

<sup>a</sup>Equivalent circuit diagram simulating the behaviour of the cell.

cedure to take into account the distributed capacitance due to the large electrode capacity. Data fitting results are shown in **Table 2**.

The series resistance (R<sub>s</sub>), above discussed, is essentially associated with the ohmic properties of the electrolyte (and electrodes), whereas the first RQ element, characterized by high relaxation frequency, is associated with the cathode process and the second and third RQ elements with low relaxation frequency are associated with the anodic and protective layer processes. The comparison between the values of R<sub>1</sub>, due to the polarization resistances for the oxygen reduction reaction (ORR), with that of R<sub>2</sub> and R<sub>3</sub>, due to the ethanol oxidation reaction (EOR), confirms the higher rate of the first reaction, as mentioned above. The admittance values assumed by the CPE in the third semicircle (Y<sub>3</sub>), in the presence of ethanol feed, are significantly larger than those observed for the first and second semicircles. Such evidence together with the much longer relaxation time associated to the third semicircle may reflect the occurrence of a mass transport control in comparison to the charge transfer phenomena related to the second and first semicircles occurring at higher frequencies [39].

Data fitting results are shown in **Table 2**. Although the strong overlapping of the semicircles makes difficult the data deconvolution, the major evidences are in line with the qualitative comments made above. Some additional considerations regard the fact that a constant phase element (CPE) is used in the fitting procedure to take into account the distributed capacitance due to the large electrode porosity. The admittance values assumed by the CPE in the third semicircle (Y<sub>3</sub>), in the presence of ethanol feed, are significantly larger than those observed for the first and second semicircles. These essentially reflect the difference of capacitance characteristics related to the mass transport in comparison to the charge transfer phenomena.

The morphology of the SOFC cell after 100 h operation shutdown under reducing conditions (i.e. 10 vol.% of H<sub>2</sub> in N<sub>2</sub>) was then investigated by SEM. **Fig. 7a-d** shows different zones of the cell cross-section at different magnifications. The aim of this analysis was to get insights on the interface between the layers and the possible presence of carbon-based deposits as consequence of the direct feed of dry ethanol. **Fig. 7a** shows the complete cell cross section. It is particularly evident the open structure of the anode support, the thin electrolyte, and the cathode layer. The anodic support is magnified in **Fig. 7b** that shows well distributed and homogeneous in size Ni-particles mixed with smaller YSZ-particles. The protective layer thickness is about 4  $\mu\text{m}$  (**Fig. 7**). **Fig. 7c** shows the interface between the protective layer and the supporting anode. **Fig. 7d** shows the almost regular morphology of the protective layer formed by composite nanosized powders. No

evidence of carbon deposits was observed for both pre-layer and supporting anode, confirming the positive role of the protective layer for operation with dry ethanol.

**Fig. 8** shows the chromatograms of the condensed liquids for the outlet stream collected during the endurance test reported in **Fig. 4** at 40 h and 106 h. These are related to the experiments carried out by feeding diluted ethanol (EtOH(g) (4.5 cc/min) + N<sub>2</sub> (35 cc/min)) at 0.8 V and concentrated ethanol (EtOH(g) (6.4 cc/min) + N<sub>2</sub> (10 cc/min)) at 0.7 V. Water and unreacted ethanol are the main species in the condensed liquid products with small traces of acetaldehyde and acetic acid. The analysis of the gas stream (**Fig. 9**) showed essentially CO<sub>2</sub>, and unreacted CO and H<sub>2</sub> together with CH<sub>4</sub> as reaction products. The relatively small concentration of ethanol in water in the condensed liquid fraction indicates that most of the ethanol is converted under electrochemical operation and H<sub>2</sub>O is a main reaction product. According to this evidence, ethanol conversion should be much higher than that estimated from the Faradic process. By decreasing the cell potential from 0.8 V to 0.7 V, the traces of acetaldehyde increase whereas the traces of acetic acid remain substantially unchanged.

**Fig. 9** shows the GC data obtained for the gas stream after the liquid trap. The data shown in the chromatogram are referred to the operation of the cell at 0.7 V where conversion of ethanol is larger. As discussed above, the main products observed in the chromatogram of the outlet gas phase are referred to unconverted H<sub>2</sub>, CO and CO<sub>2</sub>. It is noteworthy that a significant amount of methane was also recorded. Quantitative data related to the gas chromatographic analysis are reported in **Table 3**.

An additional endurance test was carried out under high voltage efficiency operating conditions (cell voltage: 0.8 V) with the lowest possible ethanol dilution (6.4 cc min<sup>-1</sup> of EtOH and 10 cc min<sup>-1</sup> of N<sub>2</sub>) by nitrogen (**Fig. 10**). The overall test duration was 500 h and included about 100 h conditioning in H<sub>2</sub> and 400 h operation with dry ethanol under the above reported operating conditions. A low degradation rate was observed under both operating conditions; the cell appears to reach a steady-state condition after about 50 h operation in the presence of a specific fuel, indicating proper stability. Also in this case no formation of carbon deposits was observed. This result shows that the specific structure of the Ni-modified perovskite is effective in promoting SOFC operation with dry ethanol.

#### 4. Discussion

From the comparison of the results obtained for the modified cell with those of the uncoated cell, it is clear that the protective layer

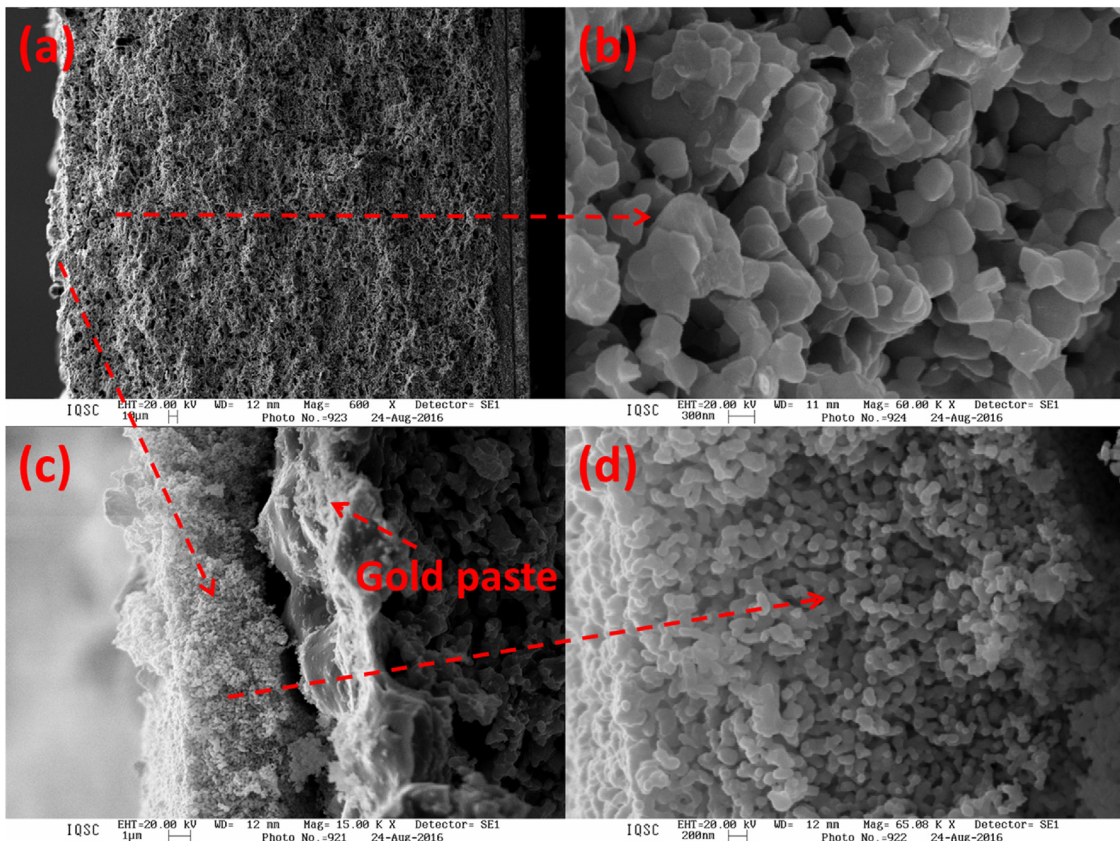


**Fig. 7.** SEM images of the SOFC cell post-operation. a) low magnification micrograph showing the entire cell; b) high magnification of inner anode support; c) details of interface between protective layer/anode support and gold current collector; d) high magnification of the inner part of the protective layer.

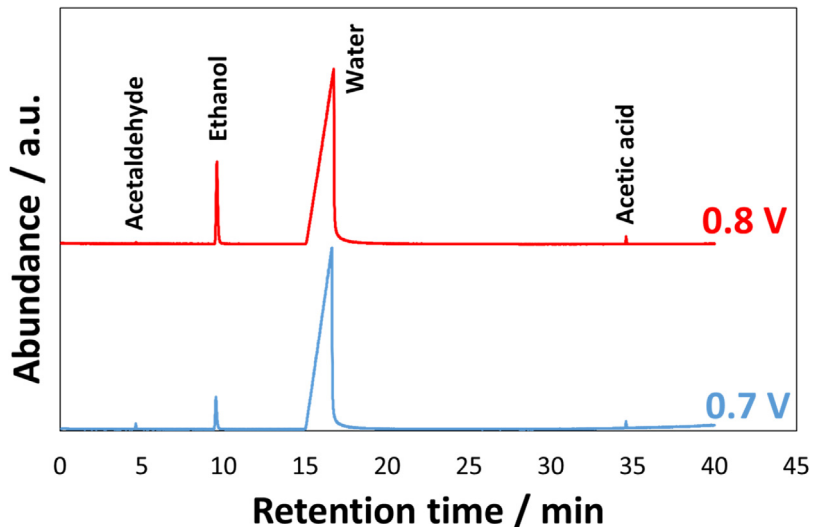


**Fig. 8.** Gas-chromatogram of outlet liquid from the anode chamber for the cell fed with dry ethanol.

plays a fundamental role in the ethanol conversion without any carbon deposition issue. In principle, ethanol dehydrogenation and cracking processes can be promoted by the presence of highly dispersed Ni clusters as well as by surface iron and cobalt atoms on the catalyst surface. In addition, ceria also contained in the composite layer, is known to possess suitable activity for conversion of organic compounds to H<sub>2</sub>, CO and CO<sub>2</sub> without carbon deposition. This is due to the excellent oxygen uptake and storage capacity of CeO<sub>2</sub> [40]. In particular, the oxygen contained in the ethanol molecule

can oxidize the reduced ceria species (CeO<sub>2-x</sub>) in CGO (Fig. S4c) and recover the oxidized state of ceria (i.e. CeO<sub>2</sub>). In other words, reduced ceria species in CGO (Fig. S4c) can break the O–H bonding and uptake the oxygen of ethanol in the substoichiometric lattice to saturate defects according to the literature [40]. In particular, it was shown in the literature that ceria associated defects may have a beneficial role by lowering the activation of the oxygen exchange "surface" [40]. This oxygen may be subsequently transferred to the formed H<sub>2</sub> molecules, from ethanol dehydrogenation on Ni-Fe-Co

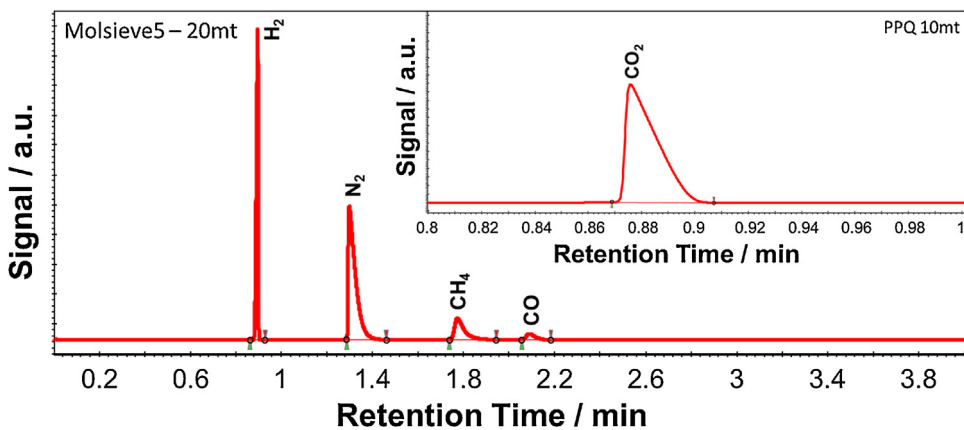


**Fig. 9.** Gas-chromatogram of the gas stream at the anode outlet after the condenser. Test carried out at 0.7 V.

**Table 3**

Gas-chromatographic analysis data for the condensed liquid and the gas phases at the outlet of the anodic SOFC chamber.

		Retention time <sup>a</sup> min	Product% @ 0.8 V	Product% @ 0.7 V
Condensed fraction	Acetaldehyde	4.636	traces	traces
	Ethanol	9.538	18.73	9.3
	Water	16.603	81.26	90.69
	Acedic Acid	34.588	traces	traces
Gas fraction	H <sub>2</sub>	0.90	6.38	6.30
	CO	2.09	3.36	3.65
	CO <sub>2</sub>	0.88	10.47	10.49
	CH <sub>4</sub>	1.77	3.98	3.96
	N <sub>2</sub>	1.30	75.81	75.60

<sup>a</sup> Retention times are referred to chromatograms in Figs. 8 and 9.

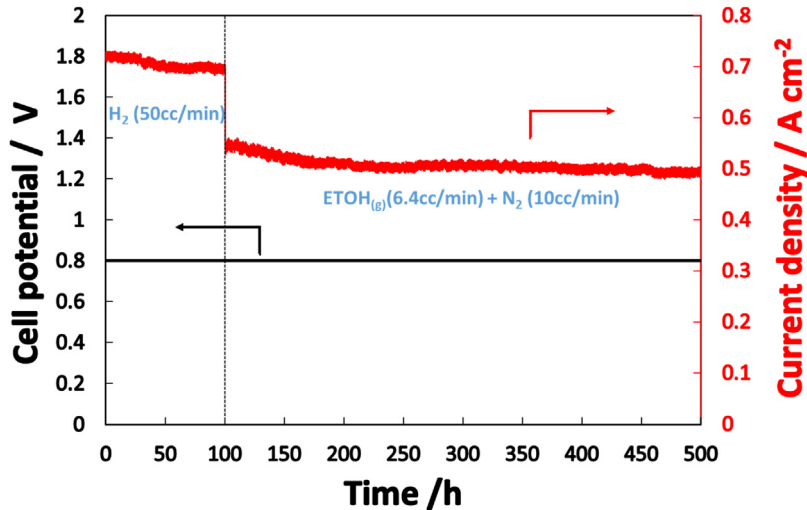
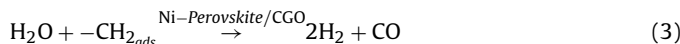
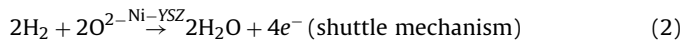
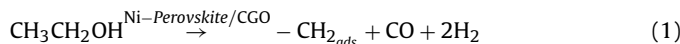


**Fig. 10.** Endurance test (400 h) carried out at 800 °C in presence of dry ethanol at the fixed potential of 0.8 V and after a prolonged conditioning procedure in pure H<sub>2</sub> (i.e. 100 h).

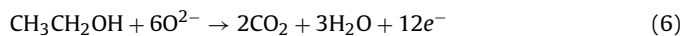
clusters, producing H<sub>2</sub>O or giving rise to CO species by reaction with adsorbed species produced by the cracking process (Reaction (1)) [41]. Very likely the water formed by the oxidation of H<sub>2</sub> permeated at Ni-YSZ interface (Reaction (2)), that is back diffusing to the pre-layer, causes internal reforming of adsorbed-CH<sub>x</sub> species to CO and H<sub>2</sub> (Reaction (3)). The growth of C nanofibers from CH<sub>x</sub> species is essentially hindered in the present case by the presence of the FeCoO<sub>x</sub> core which impedes the extensive formation of Ni-carbide species, which are often the precursors of carbon deposits [42]. Formation of rhombohedral Ni<sub>3</sub>C [43] is also hindered on the chemical and electronically modified Ni particles by the effect of the Fe-Co

oxide shell. Removal of the adsorbed carbonaceous species is thus promoted by such shuttle mechanism involving hydrogen permeation into the Ni-YSZ layer, oxidation by the ionic oxygen from the cathode (O<sup>2-</sup>), back diffusion to the pre-layer as H<sub>2</sub>O. This provides the additional oxygen that is necessary for the complete internal reforming of the organic species at the modified perovskite layer (Reaction (3)). The full oxidation reaction is made possible by permeation and oxidation at the Ni-YSZ interface of the addition H<sub>2</sub> (Reaction (4)) and CO (Reaction (5)) formed in the previous inter-

nal reforming step (Reaction (3)). The complete process is described below:



The full ethanol oxidation half-cell reaction is reported below:

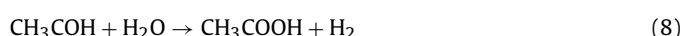


Permeation of H<sub>2</sub> and CO through the anode to the interface with the electrolyte and back diffusion of H<sub>2</sub>O and CO<sub>2</sub> can be affected by mass transport limitations as those observed in the polarization and impedance curves. These phenomena can be essentially related to the saturation of catalyst pores by reaction intermediates. On the other hand, a complete oxidation mechanism at the protective layer would require an efficient transport of O<sup>2-</sup> species along the entire anode structure and subsequent reaction with the adsorbed carbon species. However, also this mechanism can be affected by diffusion limitations. Thus, it is likely that most of O<sup>2-</sup> ions from the cathode after migration through the ceramic membrane, according to the SOFC operating mechanism, react at the Ni-YSZ interface with syngas formed at the modified perovskite layer and permeated through the porous electrode to the interlayer with the dense YSZ electrolyte [44,45]. The fact that CO and H<sub>2</sub> species are observed in the gas chromatogram in relevant amounts would indicate that mass transport limitations impede some of these molecules to diffuse at the Ni-YSZ interface. Accordingly, some of these molecules are released into the anode chamber without contributing to the Faradaic process. This explains why ethanol conversion from gas chromatographic analysis appears much higher than Faradaic conversion. Of course, this issue can be greatly mitigated in large area cells and stacks where there is no need to feed the fuel in large excess as in the present case. However, such evidence also shows the capability of this pre-layer to operate at very high gas hourly space velocity (GHSV).

Besides the above discussed reaction mechanism involving dehydrogenation and cracking processes as initial steps, the presence of traces of acetaldehyde, acetic acid and methane in the chromatographic analysis would indicate another parallel or competitive catalytic reaction. This can involve a partial dehydrogenation the hydroxyl group of ethanol to form acetaldehyde (Reaction (7)).



The produced hydrogen diffuses to the Ni-YSZ layer where it is oxidized by the ionic oxygen (O<sup>2-</sup>) and returns as H<sub>2</sub>O in the perovskite layer. The fact that water was observed in the GC analysis and only a dry fuel was fed to the cell indicates that only part of the formed water contributes to the pre-reforming process. At 800 °C a fast diffusion of water from the Ni-electrolyte interface to the outlet gas stream through the porous anode layer appears reasonable (Reaction (8)):



Acetic acid can give rise to a fast cracking process producing adsorbed –CH<sub>2</sub> species, CO<sub>2</sub> and H<sub>2</sub>. The adsorbed CH<sub>2</sub> species can be internally reformed (Reaction (9)) to CO and H<sub>2</sub> by the water back diffusing from Ni-YSZ:



Alternatively, acetic acid can decompose into methane and CO<sub>2</sub> (Reaction (10)).



This reaction is particularly fast if it is assisted by a catalyst support characterized by basic surface properties [46] such as the presently modified perovskite. In a previous report, we have shown that the anode doping with Ba can effectively increase the basicity of the electrocatalyst and mitigate carbon deposition [35]. This is here corroborated by the increased occurrence of alkaline species (Sr) on the perovskite surface in the reduced pre-layer. The fraction of CH<sub>4</sub> that is not internally reformed (Reaction (10)) is released into the anode chamber and observed in the gas phase. However, the latter mechanism does not involve CO as reaction intermediate; whereas, this specie is also observed in the gas-chromatogram in accordance to the first mechanism here postulated. This further supports the occurrence of at least two reaction mechanisms.

Also, the second mechanism suggests that the modified perovskite pre-layer and the Ni-YSZ electrode play different roles, i.e. ethanol substrate activation and internal reforming occur at the modified perovskite layer, and syngas electrochemical oxidation occurs at the Ni-YSZ thus avoiding the formation of carbon deposits. The absence of carbon deposition from adsorbed CH<sub>x</sub> species [47] is made possible by the presence of dispersed nanosized particles consisting of FeOx shell and enriched Ni-alloy and the high surface basicity [35] of the pre-layer electrocatalyst. On the other hand, the mixed ionic-electronic conducting (MIEC) properties of support based on SrFeLaO<sub>4</sub> having a Ruddlesden-Popper phase allows both electronic and electronic percolation resulting in promising performances for the dry ethanol fed SOFC.

Accordingly to the data reported in Table 3, an increased consumption of ethanol corresponding to a higher H<sub>2</sub>O/EtOH ratio is observed when the cell is operated at 0.7 V. The increase of ethanol conversion at lower cell potentials is related to an increased rate of the electrochemical process produced by the larger anode overpotential according to the Volmer-Butler equation. The larger overpotential promotes a faster consumption of H<sub>2</sub> and CO through an increased provision of O<sup>2-</sup> ions from the cathode. This shifts the reaction equilibrium toward the oxidation products.

## 5. Conclusions

The present work explores a simple approach for the direct utilization of dry ethanol in SOFCs while avoiding both external fuel processing and relevant modifications of conventional planar ceramic cells. Such approach is based on the use of a protective layer coated on the supporting anode. This promotes an in-situ fuel processing thus avoiding that unreacted ethanol or large molecular weight organic intermediates give rise to a cracking process with consequent carbon deposition at the supporting Ni-YSZ anode. The pre-layer is essentially a multifunctional catalyst combining the properties of C–C bond cleavage of nanosized Ni particles enriched of FeOx in the outermost layers, with the oxygen ion transport and electronic conductivity of the perovskite, and the oxygen storage/release properties of ceria. Carbon fibers formation and growth mechanisms are hindered by the absence of metallic Ni on the outer surface. This work proves that the utilization of dry ethanol directly fed to the anode chamber of a modified commercial-type cell is possible while achieving suitable performance (up to 650 mW cm<sup>-2</sup>) at high voltage efficiency.

Two main reaction mechanisms are suggested to explain the absence of carbon deposits. One is proceeding through an initial dehydrogenation of ethanol at the protective layer followed by cracking and conversion to syngas. Hydrogen is oxidized to water by O<sup>2-</sup> ions after permeation in the Ni-YSZ layer. The water back-

diffusing from the Ni-YSZ layer to the protective layer produces an internal reforming. Alternatively, a partial dehydrogenation of ethanol may occur at the pre-layer giving rise to acetaldehyde that is converted to acetic acid by water back-diffusing from Ni-YSZ according to the above mechanism. Subsequent decomposition of acetic acid to CH<sub>4</sub> and CO<sub>2</sub> may occur as suggested by chromatographic analysis. A shuttle mechanism involving permeation of H<sub>2</sub>, from the dehydrogenation process, into the Ni-YSZ layer and returning at the protective layer as H<sub>2</sub>O, to promote internal reforming or oxidation of acetaldehyde, is essential in both reaction pathways and avoids carbon deposition. This is further mitigated by the surface basicity of the modified perovskite.

## Acknowledgements

The present work was in part carried out in the framework of the Research Program promoted by the Brazilian “Conselho Nacional de Desenvolvimento Científico e Tecnológico” entitled “Ciência sem Fronteiras” processo n° 402180/2012-7. Authors also would like to thank Fundação de Amparo a Pesquisa do Estado de São Paulo (proc. 2013/16930-7), Brazil for financial assistances. Dr. Rafael Machado Reis thanks FAPESP agency for post-doctoral fellowship (FAPESP Proc. 2014/04100-2). N.H. and F.R.Z. gratefully acknowledge the financial support of the Slovenian Research Agency (ARRS) through the Research Core Funding Programme P2-0152, P2-0393 and Project Z2-8161.

The CNR authors acknowledge the Italian Ministry of Research and Education for the financial support of the BIOITSOFC project within the program ‘PROGRAMMI DI RICERCA SCIENTIFICA DI RILEVANTE INTERESSE NAZIONALE-PRIN PROGRAMMA DI RICERCA – Anno 2010–2011 – prot. 2010KHLKFC’.

The authors also thank Mr. Giuseppe Monforte for the XPS analysis.

## Appendix A. Supplementary data

Supplementary data associated with this article can be found, in the online version, at <http://dx.doi.org/10.1016/j.apcatb.2017.08.010>.

## References

- [1] P.E. Tsiakaras, J. Power Sour. 171 (2007) 107–112.
- [2] S.L. Douvartzides, F.A. Coutelieris, P.E. Tsiakaras, J. Power Sour. 114 (2003) 203–212.
- [3] M. Dokuya, Solid State Ionics 152–153 (2002) 383–392.
- [4] T. Guo, X. Dong, M.M. Shirodkar, X. Song, M. Wang, L. Zhang, M. Li, H. Wang, ACS Appl. Mater Interfaces 6 (2014) 16131–16139.
- [5] W. Wang, C. Su, Y. Wu, R. Ran, Z. Shao, Chem. Rev. 113 (2013) 8104–8151.
- [6] Y. Kim, J.H. Kim, J. Bae, C.W. Yoon, S.W. Nam, J. Phys. Chem. C 116 (2012) 13281–13288.
- [7] W. Wang, H. Zhu, G. Yang, H.J. Park, D.W. Jung, C. Kwak, Z. Shao, J. Power Sour. 258 (2014) 134–141.
- [8] A.A.A. da Silva, N. Bion, F. Epron, S. Baraka, F.C. Fonseca, R.C. Rabelo-Neto, L.V. Mattos, F.B. Noronha, Appl. Catal. B: Environ. 206 (2017) 626–641.
- [9] M. Lo Faro, R.M. Reis, G.G.A. Saglietti, S.C. Zignani, S. Trocino, P. Frontera, P.L. Antonucci, E.A. Ticianelli, A.S. Aricò, J. Appl. Electrochem. 45 (2015) 647–656.
- [10] W. Wang, C. Su, T. Zheng, M. Liao, Z. Shao, Int. J. Hydrogen Energy 37 (2012) 8603–8612.
- [11] J.T.S. Irvine, A. Sauvet, Fuel Cells 1 (2001) 205–210.
- [12] H.-Y. Chang, S.-H. Wang, Y.-M. Wang, C.-W. Lai, C.-H. Lin, S.-Y. Cheng, Int. J. Hydrogen Energy 37 (2012) 7771–7778.
- [13] P.I. Cowin, C.T.G. Petit, R. Lan, J.T.S. Irvine, S. Tao, Adv. Energy Mater. 1 (2011) 314–332.
- [14] Y.-H. Huang, R.I. Dass, Z.-L. Xing, J.B. Goodenough, Science 312 (2006) 254–257.
- [15] M.R. Goldwasser, M.E. Rivas, M.L. Lugo, E. Pietri, J. Pérez-Zurita, M.L. Cubeiro, A. Griboval-Constant, G. Leclercq, Catal. Today 107–108 (2005) 106–113.
- [16] S. Tao, J.T.S. Irvine, Nat. Mater. 2 (2003) 320–323.
- [17] A. Sin, E. Kopnin, Y. Dubitsky, A. Zaopo, A.S. Aricò, L.R. Gullo, D.L. Rosa, V. Antonucci, J. Power Sour. 145 (2005) 68–73.
- [18] O. Kwon, S. Sengodan, K. Kim, G. Kim, H.Y. Jeong, J. Shin, Y.-W. Ju, J.W. Han, G. Kim, Nat. Commun. 8 (2017) 1–7.
- [19] S. Sengodan, S. Choi, A. Jun, T.H. Shin, Y.-W. Ju, H.Y. Jeong, J. Shin, J.T.S. Irvine, G. Kim, Nat. Mater. 14 (2015) 205–209.
- [20] S. Kim, A. Jun, O. Kwon, J. Kim, S. Yoo, H.Y. Jeong, J. Shin, G. Kim, ChemSusChem 8 (2015) 3153–3158.
- [21] D. Neagu, T.-S. Oh, D.N. Miller, H. Ménard, S.M. Bukhari, S.R. Gamble, R.J. Gorte, J.M. Vohs, J.T.S. Irvine, Nat. Commun. 6 (2015) 1–8.
- [22] D. Neagu, G. Tsekouras, D.N. Miller, H. Ménard, J.T.S. Irvine, Nat. Chem. 5 (2013) 916–923.
- [23] G. Yang, W. Zhou, M. Liu, Z. Shao, ACS Appl. Mater Interfaces 8 (2016) 35308–35314.
- [24] C. Arrivé, T. Delahaye, O. Joubert, G. Gauthier, J. Power Sour. 223 (2013) 341–348.
- [25] N. Wu, W. Wang, Y. Zhong, G. Yang, J. Qu, Z. Shao, ChemElectroChem 4 (2017) 1–8.
- [26] R. Montanini, F. Freni, G.L. Rossi, Rev. Sci. Instrum. 83 (2012) 1–8.
- [27] L. Zhu, B. Wei, Y. Zhang, Z. Lü, Z. Wang, X. Huang, Z. Cao, W. Jiang, Y. Li, Electrochim. Acta 160 (2015) 89–93.
- [28] S. Kogler, A. Nenning, G.M. Rupp, A.K. Opitz, J. Fleig, J. Electrochem. Soc. 162 (2015) F317–F326.
- [29] R.D.L. Smith, M.S. Prévot, R.D. Fagan, Z. Zhang, P.A. Sedach, M.K.J. Siu, S. Trudel, C.P. Berlinguet, Science 340 (2013) 60–63.
- [30] R.D.L. Smith, M.S. Prévot, R.D. Fagan, S. Trudel, C.P. Berlinguet, J. Am. Chem. Soc. 135 (2013) 11580–11586.
- [31] C.G. Morales-Guio, L. Liardet, X. Hu, J. Am. Chem. Soc. 138 (2016) 8946–8957.
- [32] S.K. Vaipai, B.V. Mahesh, R.K. Dube, J. Alloys Compd. 476 (2009) 311–317.
- [33] Z. Yu, D. Chen, M. Rønning, T. Vrålstad, E. Ochoa-Fernández, A. Holmen, Appl. Catal. A: Gen. 338 (2008) 136–146.
- [34] J.F. Moulder, W.F. Stickle, P.E. Sobol, Handbook of X-ray Photoelectron Spectroscopy: a Reference Book of Standard Spectra for Identification and Interpretation of XPS Data, Physical Electronics, Inc., Eden Prairie, Minn, 1995.
- [35] D. La Rosa, A. Sin, M. Lo Faro, G. Monforte, V. Antonucci, A.S. Aricò, J. Power Sour. 193 (2009) 160–164.
- [36] J.-W. Kim, A.V. Virkar, K.-Z. Fung, K. Mehta, S.C. Singhal, J. Electrochem. Soc. 146 (1999) 69–78.
- [37] M. Lo Faro, S. Trocino, S.C. Zignani, A.S. Aricò, G. Maggio, C. Italiano, C. Fabiano, L. Pino, A. Vita, Int. J. Hydrogen Energy 41 (2016) 5741–5747.
- [38] R. Barfod, M. Mogensen, T. Klemensø, A. Hagen, Y.L. Liu, P. Vang Hendriksen, J. Electrochem. Soc. 154 (2007) B371–B378.
- [39] R. Mohammadi, M. Ghassemi, Y.M. Barzi, J. Pirkandi, J. Solid State Electrochem. 18 (2014) 2815–2827.
- [40] N. Yang, Y. Shi, S. Schweiger, E. Strelcov, A. Belianinov, V. Foglietti, P. Orgiani, G. Balestroino, S.V. Kalinin, J.L.M. Rupp, C. Aruta, ACS Appl. Mater Interfaces 8 (2016) 14613–14621.
- [41] F. Frusteri, G. Italiano, C. Espro, C. Cannilla, G. Bonura, Int. J. Hydrogen Energy 37 (2012) 16367–16374.
- [42] S. Helveg, C. Lopez-Cartes, J. Sehested, P.L. Hansen, B.S. Clausen, J.R. Rostrup-Nielsen, F. Abild-Pedersen, J.K. Norskov, Nature 427 (2004) 426–429.
- [43] X. Chen, T. Saito, M. Kusunoki, S. Motojima, J. Mater. Res. 14 (1999) 4329–4336.
- [44] M.D. Gross, J.M. Vohs, R.J. Gorte, J. Electrochem. Soc. 154 (2007) B694–B699.
- [45] K. Chen, X. Chen, Z. Lü, N. Ai, X. Huang, W. Su, Electrochim. Acta 53 (2008) 7825–7830.
- [46] L.V. Mattos, F.B. Noronha, J. Catal. 233 (2005) 453–463.
- [47] K. Tomishige, O. Yamazaki, Y. Chen, K. Yokoyama, X. Li, K. Fujimoto, Catal. Today 45 (1998) 35–39.